第 43 卷 第 2 期/2023 年 1 月/光学学报 研究论文

光学学报

嵌入式相位传感的多功能Stokes-Mueller偏振仪

钟慧，李艳秋**，刘克*，王嘉智，李员赫，吴劲贤

北京理工大学光电学院光电成像技术与系统教育部重点实验室，北京 100081

摘要 Mueller矩阵因可以定量地提供组织样品的完整偏振信息，已被广泛地应用于癌症的病理诊断中。现有的Mueller成像偏振检测仪器丢失了样品的绝对相位信息，而相对的相位信息不能反映待测相位的变化规律，故需要开发嵌入式偏振光波前绝对相位检测仪器。搭建了一款嵌入式相位传感的Stokes-Mueller偏振仪，将研发的四波横向剪切干涉仪集成在偏振仪中，不仅实现了生物样品偏振信息的提取，还实现了样品相位信息和折射率的实时测量。以肺癌组织切片为研究对象，通过对退偏参数和折射率值的比较准确地实现了对正常区域和癌变区域的识别。所提技术丰富了偏振仪的测量功能，通过测量绝对相位实现了样品折射率的测量，进而能够为癌症诊断领域提供一种更全面的辅助手段。

关键词 测量；偏振；Mueller矩阵；相位测量；折射率；定量

中图分类号 O436.3 **文献标志码** A **DOI**：10.3788/AOS221272

1 引 言

由于偏振成像技术可以提取更丰富的样品结构和光学信息，且对亚波长微观结构变化也非常敏感，故该方法在生物医学，尤其是肿瘤癌症检测领域中表现出了很好的应用前景[1-3]。其中，Mueller矩阵成像方法通过对Mueller矩阵进行分解和变换将Mueller矩阵转化为具有明确物理意义的参数，这样就能够对生物组织及其病变部位进行更加明确的定性分析。因此，它已被广泛用于检测各种癌症，如宫颈癌[4-5]、皮肤癌[6-7]和肝癌[8-9]等。

Oldenbour[10-11]将偏振技术和传统光学显微镜相结合，设计了采用液晶可调波片的新型偏振显微镜，该器件被广泛用于生物细胞形态的检测中。de Martino等[12-15]研发了多光谱Mueller成像仪，并用于癌症的早期诊断、检测，以及肿瘤复发的监测中。Wang等[16-20]研发了Mueller显微镜，并对多种癌变组织切片（结肠、皮肤和肌腱等）进行了偏振测量，利用标定后不同数值孔径（NA）的物镜实现了癌症组织和细胞层面的高精度Stokes-Mueller成像检测。He等[21-25]研发了基于Mueller矩阵的全偏振显微镜，并将其应用于癌组织病理的诊断、分期等方面中，展现出了良好的使用效果。然而，以上所使用的Mueller偏振仪都丢失了生物样品的绝对相位信息，而连续的绝对相位信息才能反映被测量的变化。

绝对相位作为光的基本属性，可以量化由样品物理厚度和折射率系数决定的相位特性。其中，折射率作为生物样品最重要的光学属性之一，已有研究表明其可用来描述生物组织的光学特性和对病变组织进行评估[26-28]，具有重大的研究价值。四波横向剪切干涉技术作为绝对相位检测方法之一，因其具有无需额外的波前参考光、对光源无特殊要求和结构简单等优点，非常适合用于相位显微成像和样品绝对相位信息的测量[29-31]。然而，目前鲜有关于四波横向剪切干涉仪用于癌组织病理诊断的研究报道，故需要开发嵌入式偏振光波前绝对相位检测仪器，以满足各类不同样品的检测需求。

针对上述问题，本研究团队提出了一种嵌入式相位传感的Stokes-Mueller偏振技术，将课题组自主研制的全局随机编码四波横向剪切干涉仪集成在Mueller偏振仪中，解决了Mueller矩阵偏振仪测量结果中绝对相位缺失的问题，在实现生物样品偏振信息提取的同时，通过绝对相位值实现了折射率的测量，提供了新的定量诊断指标，丰富了偏振仪的测量功能。所搭建的嵌入式相位传感的Stokes-Mueller成像偏振仪是传统Mueller偏振成像仪的一个功能扩展。定量分析表明，将所提方法应用于肺癌切片的测量中，通过对退偏和折射率的信息的比较，可以准确实现对正常区域和癌变区域的识别，有望为医学提供更全面的辅助诊断手段。

2 基本原理

2.1 Mueller矩阵理论基础

考虑到生物组织如细胞等具有显著的散射特性，

收稿日期：2022-06-07；**修回日期**：2022-07-11；**录用日期**：2022-07-18；**网络首发日期**：2022-07-28

基金项目：国家自然科学基金（11627808）

通信作者：*liuke@bit.edu.cn；**liyanqiu@bit.edu.cn

目前通常采用Mueller矩阵来描述偏振光。每束光波的光强和偏振态都可以用Stokes矢量的4个参数来描述，即

$$S=\begin{bmatrix} I \\ Q \\ U \\ V \end{bmatrix}=\begin{bmatrix} E_{ox}^2+E_{oy}^2 \\ E_{ox}^2-E_{oy}^2 \\ 2E_{ox}E_{oy}\cos(\varphi_y-\varphi_x) \\ 2E_{ox}E_{oy}\sin(\varphi_y-\varphi_x) \end{bmatrix}, \tag{1}$$

式中：E_{ox}和E_{oy}是垂直于传播方向的两个正交复电场分量；φ_x是E_{ox}的相位；φ_y是E_{oy}的相位。令$\boldsymbol{S}_o$和$\boldsymbol{S}_i$分别是输出光与输入光的Stokes矢量，光与散射介质之间的这种相互作用可表述为Stokes矢量与大小为4×4的矩阵$\boldsymbol{M}$的乘积，即$\boldsymbol{S}_o=\boldsymbol{M}\cdot\boldsymbol{S}_i$。$\boldsymbol{M}$也被称为散射介质的Mueller矩阵[3]，其表达式为

$$\boldsymbol{M}=\begin{bmatrix} m_{11} & m_{12} & m_{13} & m_{14} \\ m_{21} & m_{22} & m_{23} & m_{24} \\ m_{31} & m_{32} & m_{33} & m_{34} \\ m_{41} & m_{42} & m_{43} & m_{44} \end{bmatrix}。 \tag{2}$$

Mueller矩阵的16个元素包含了大量被测样品的偏振结构信息，为了建立起Mueller矩阵元素与介质偏振特性之间的关系，采用极分解法将Mueller矩阵分解为三个矩阵的乘积[3]，即

$$\boldsymbol{M}=\boldsymbol{M}_\Delta\cdot\boldsymbol{M}_R\cdot\boldsymbol{M}_D, \tag{3}$$

式中：$\boldsymbol{M}_\Delta$、$\boldsymbol{M}_R$和$\boldsymbol{M}_D$是与退偏、总相位延迟和二向色性相关的矩阵。利用分解得到的子矩阵可进一步推导得到退偏Δ、总相位延迟R和二向色性D的表达式分别为

$$\Delta=1-\frac{\left|\mathrm{tr}(\boldsymbol{M}_\Delta)-1\right|}{3}, \tag{4}$$

$$R=\arccos\left[\frac{\mathrm{tr}(\boldsymbol{M}_R)}{2}-1\right], \tag{5}$$

$$D=\sqrt{m_{12}^2+m_{13}^2+m_{14}^2}, \tag{6}$$

式中：tr(•)为迹函数。

2.2 相位延迟与绝对相位

从式(1)和式(5)可以看出，Mueller矩阵不保留偏振光相位的绝对信息，只包含偏振光相位延迟信息。从式(1)可以得出$\varphi_y-\varphi_x=\varphi$，由于相位2π的周期性，故$\varphi$的取值范围为−π～π，如图1(a)所示。同样，式(5)的相位延迟量R可由反余弦函数得到，故获得的相位值不连续，被截断在[0, π]区域内，如图1(b)所示。可以看出，Mueller矩阵提取出的相位差值因其计算三角函数值域的限制，相位产生截断，不能提取出绝对相位，故被测量常常是与连续的绝对相位分布相关联的。

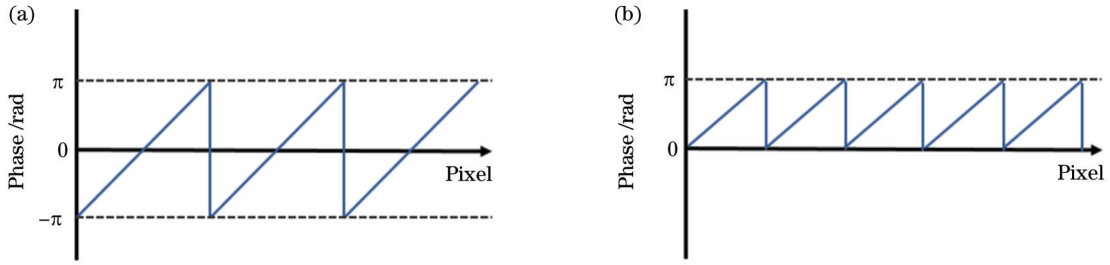

图1 缠绕相位图。(a)相位差φ；(b)相位延迟R

Fig. 1 Wrapping phase diagram. (a) Phase difference φ; (b) phase retardance R

对某一种偏振光变换来说，仅考虑这两分量的差，即相位延迟量就足够了，但若可以测得绝对相位信息，就可根据相位与光程差的关系推导出偏振成像无法获得的组织折射率。然而，已有研究表明，折射率作为描述介质光学性质的基本参数，在生物组织光学研究中起着非常重要的作用[26-28]。因此，分别考虑绝对相位和相对相位差是很有意义的。为了解决以上问题，本文提出了嵌入式的相位传感技术，系统的搭建和测量过程会在2.3节中进行详细介绍。将课题组自主研发的四波横向剪切干涉仪集成在偏振仪中，利用剪切干涉仪来实现绝对相位信息的测量，原理如图2所示。待测波前通过光栅后被主要衍射为(1,1)、(1,−1)、(−1,−1)和(−1,1)4束光波，4个箭头表示光波的不同传播方向。这4束光波之间存在一定的夹角，且光波性质相同，故会在探测器电荷耦合器件(CCD)平面处重叠区域内相互干涉形成剪切干涉图。

4束1级衍射光在CCD观测面上的光强分布函数可表示为

$$\begin{aligned} I(x,y)=&4E_0^2+2E_0^2\cos\left(2\pi f_0x+\Delta W_{14}\right)+2E_0^2\cos\left(2\pi f_0x+\Delta W_{23}\right)+\\ &2E_0^2\cos\left(2\pi f_0y+\Delta W_{12}\right)+2E_0^2\cos\left(2\pi f_0y+\Delta W_{34}\right)+\\ &2E_0^2\cos\left[2\pi f_0(x-y)+\Delta W_{24}\right]+2E_0^2\cos\left[2\pi f_0(x+y)+\Delta W_{13}\right], \end{aligned} \tag{7}$$

式中：E_0为4束1级衍射光的最大复振幅；f_0为x方向和y方向的空间载频；ΔW_{ij}为i号和j号衍射光的剪切波前。

式(7)可用复振幅表示为

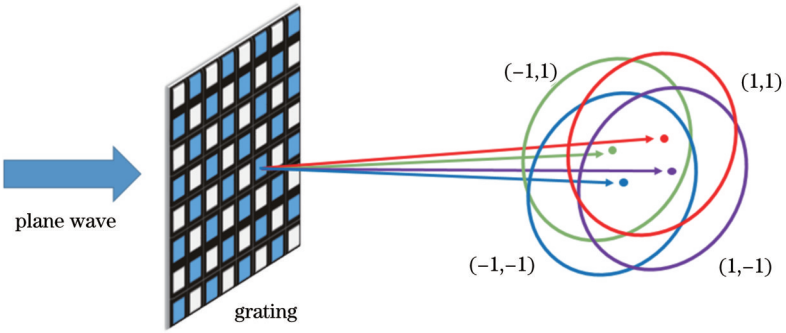

图 2 四波横向剪切干涉仪原理图

Fig. 2 Schematic diagram of quadriwave lateral shearing interferometry

$$
\begin{aligned}
I(x,y)=&4E_0^2+C_{14}\exp\left(\mathrm{i}2\pi f_0x\right)+C_{14}^*\exp\left(-\mathrm{i}2\pi f_0x\right)+C_{23}\exp\left(\mathrm{i}2\pi f_0x\right)+\\
&C_{23}^*\exp\left(-\mathrm{i}2\pi f_0x\right)+C_{12}\exp\left(\mathrm{i}2\pi f_0y\right)+C_{12}^*\exp\left(-\mathrm{i}2\pi f_0y\right)+\\
&C_{34}\exp\left(\mathrm{i}2\pi f_0y\right)+C_{34}^*\exp\left(-\mathrm{i}2\pi f_0y\right)+C_{24}\exp\left[\mathrm{i}2\pi f_0(x-y)\right]+\\
&C_{24}^*\exp\left[-\mathrm{i}2\pi f_0(x-y)\right]+C_{13}\exp\left[\mathrm{i}2\pi f_0(x+y)\right]+C_{13}^*\exp\left[-\mathrm{i}2\pi f_0(x+y)\right],
\end{aligned}
\tag{8}
$$

式中：$C_{ij}=E_0^2\exp(\mathrm{i}\Delta W_{ij})$，且 C_{ij} 与 C_{ij}^* 为共轭关系。对式(8)进行傅里叶变换，可得

$$
\begin{aligned}
\mathcal{F}\left[I(x,y)\right]=&\mathcal{F}(4E_0^2)+\mathcal{F}(C_{14}+C_{23})\otimes\delta(u-f_0,v)+\mathcal{F}(C_{14}^*+C_{23}^*)\otimes\delta(u+f_0,v)+\\
&\mathcal{F}(C_{12}+C_{34})\otimes\delta(u,v-f_0)+\mathcal{F}(C_{12}^*+C_{34}^*)\otimes\delta(u,v+f_0)+\mathcal{F}(C_{24})\otimes\delta(u-f_0,v+f_0)+\\
&\mathcal{F}(C_{24}^*)\otimes\delta(u+f_0,v-f_0)+\mathcal{F}(C_{13})\otimes\delta(u-f_0,v-f_0)+\mathcal{F}(C_{13}^*)\otimes\delta(u+f_0,v+f_0),
\end{aligned}
\tag{9}
$$

式中：$\mathcal{F}(\cdot)$ 为傅里叶变换运算符；$\delta(\cdot)$ 为狄拉克函数；(u,v) 为频域坐标；$\otimes$ 为卷积运算。根据式(9)，从 x 方向和 y 方向 1 级频谱中提取出的包裹相位可表示为

$$
\begin{cases}
\Delta\varphi_x=\arctan\left\{\dfrac{\mathrm{Im}\left\{E_0^2\left[\exp\left(\mathrm{i}2\pi f_0x+\mathrm{i}\Delta W_{x1}\right)+\exp\left(\mathrm{i}2\pi f_0x+\mathrm{i}\Delta W_{x2}\right)\right]\right\}}{\mathrm{Re}\left\{E_0^2\left[\exp\left(\mathrm{i}2\pi f_0x+\mathrm{i}\Delta W_{x1}\right)+\exp\left(\mathrm{i}2\pi f_0x+\mathrm{i}\Delta W_{x2}\right)\right]\right\}}\right\}\\
\Delta\varphi_y=\arctan\left\{\dfrac{\mathrm{Im}\left\{E_0^2\left[\exp\left(\mathrm{i}2\pi f_0y+\mathrm{i}\Delta W_{y1}\right)+\exp\left(\mathrm{i}2\pi f_0y+\mathrm{i}\Delta W_{y2}\right)\right]\right\}}{\mathrm{Re}\left\{E_0^2\left[\exp\left(\mathrm{i}2\pi f_0y+\mathrm{i}\Delta W_{y1}\right)+\exp\left(\mathrm{i}2\pi f_0y+\mathrm{i}\Delta W_{y2}\right)\right]\right\}}\right\}
\end{cases},
\tag{10}
$$

式中：$\mathrm{Im}(\cdot)$ 为取虚部函数；$\mathrm{Re}(\cdot)$ 为取实部函数。可以看出，因反正弦函数计算时存在阈值限制，故提取出来的相位会产生相位混叠，如图 3(a)所示。因此，本文采用质量图导引法[32-33]对包裹相位进行解包裹以恢复真实相位，实际过程就是对每个像素点增加或者减少整数个 2π，从初始点的相位值开始执行求和运算以获得连续的绝对相位，如图 3(b)所示。

由于细胞各组成部分的厚度与折射率分布存在差异，故通过样品的光的相位也会发生变化，该相位变化即为相移，其中折射率可以表征细胞内部的细节结构和特征的改变，是非常重要的物理参量。根据相位与光程差的关系，以空气为参比，可计算出样品的折射率为

$$
n=\frac{\phi\cdot\lambda}{2\pi\cdot d}+1,
\tag{11}
$$

式中：ϕ 为样品的相位值；λ 为波长；d 为样品厚度。基于测得的绝对相位信息，根据式(11)即可推导出偏振成像无法获得的组织折射率。

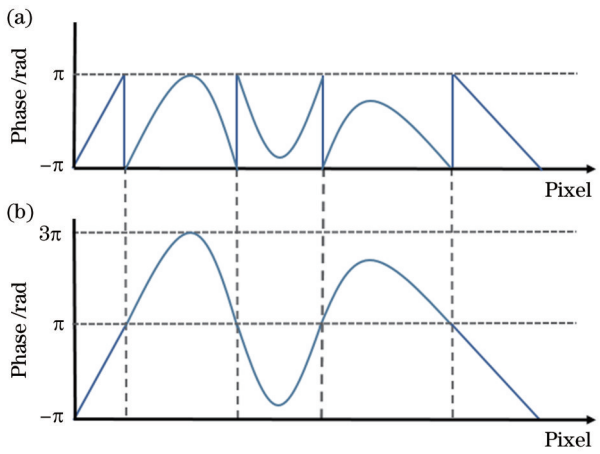

图 3 相位图。(a)包裹相位；(b)绝对相位

Fig. 3 Phase diagram. (a) Wrapping phase; (b) absolute phase

Mueller 矩阵分解法已被应用于透射方向的偏振测量中，适合用来表征病理切片样品的偏振特性，但其

不保留绝对相位信息，而相位传感技术可测得绝对相位，并可进一步表征样品的折射率。因此，本文将偏振和相位信息结合以满足多维参数偏振特性的检测要求，并且该技术可以获得样品的完整偏振特性和相位，表征样品丰富的微观结构和光学信息，可为生物医学辅助诊断提供更全面的技术手段。

2.3 系　　统

测量相位用的相位探测器是实验室自主研发的四波横向剪切干涉仪。此干涉仪共光路，对光源无特殊要求，可用常规的显微镜光源，且精度高，结构简单，不需要单独的理想参考波面，故在传统明场显微镜上使用此干涉仪无需修改光路。此外，该干涉仪不仅与Mueller偏振成像仪兼容，还互补。

本研究中使用的嵌入式相位传感的Stokes-Mueller成像偏振仪主要由光源模板[发光二极管(LED)和滤波片]、照明和成像模块(聚光镜和物镜)、偏振态产生器(PSG)和偏振态分析器(PSA)组成的偏振调制器模块，以及图像检测模块(彩色相机和相位探测器)组成，如图4所示。LED发出的光先通过滤波片，再通过PSG，PSG由线偏振片和1/4波片组成。具有特定偏振态的偏振光通过聚光镜聚焦到样品上，光束穿过样品后，利用物镜收集带有样品偏振信息的出射光，并利用PSA对PSG产生的偏振光经过样品后的偏振态进行分析，PSA由1/4波片和线偏振片组成。最后，利用彩色相机接收出射光并成像，获得了16个光强值，利用MATLAB求解出样品的Mueller矩阵和极分解后的偏振参数。同样，利用相位探测器接收含有样品折射率分布信息的出射光并在成像面进行剪切干涉，最后根据采集到的干涉图利用MATLAB重建样品相位分布，并计算出折射率。

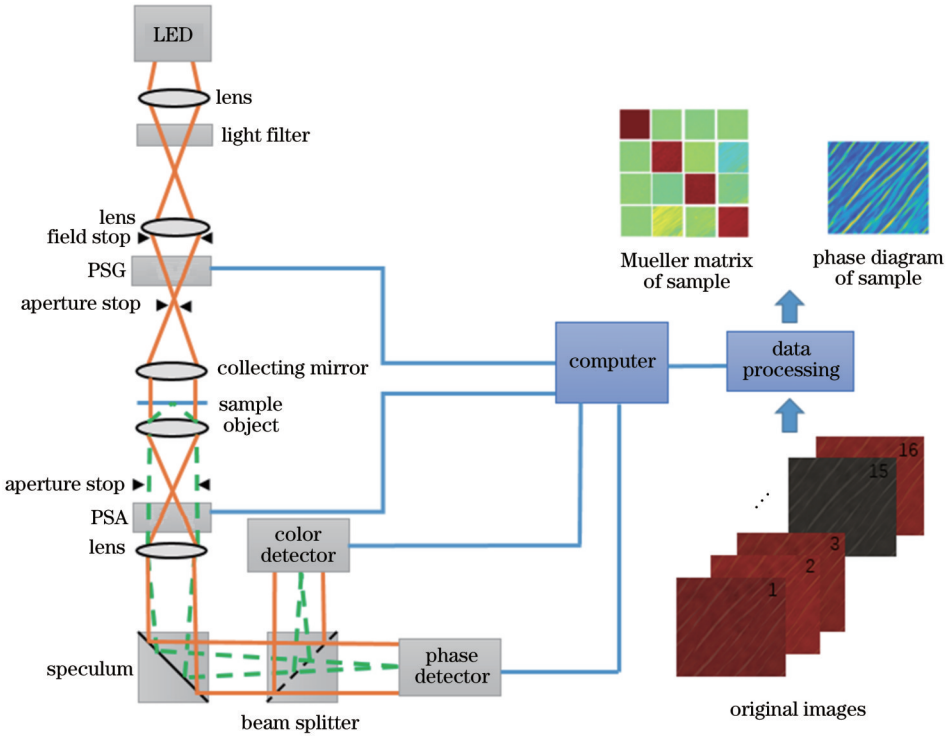

图4　嵌入式相位传感的Stokes-Mueller成像偏振仪的工作原理图

Fig. 4　Schematic diagram of Stokes-Mueller imaging polarimeter with embedded phase sensor

3　实验分析

实验装置包括Thorlabs SOLIS-3C高功率自然白光光源、Nikon C-SWA摇出式消色差聚光镜、滤光片转盘(波长为600、633、700 nm)、Nikon消色差显微物镜(放大倍数为40，NA=0.95)、Newport 10LP-VIS-B精密线偏振片、Thorlabs AQWP10M-580消色差1/4波片、AVT Manta G507C彩色相机和自主研发的四波横向剪切干涉仪。在实验中，将厚度为4 μm的肺癌组织切片作为待测样品，所用切片由北京中科万邦生物科技有限公司提供。截取尺寸为1000 pixel×1000 pixel的正方形区域为感兴趣区域以排除四角遮拦对成像结果的干扰。

本文分别选取了肺癌切片中正常和癌变区域各10个位置进行偏振和相位测量。图5和图6为633 nm波长下，其中1个位置处的Mueller极分解图像和相位图像。可以看出，不同区域的细胞形态和排列都不一样，癌变细胞排列紊乱，且因细胞过度增殖，细胞数量异常增多。从图5(b)、(e)可以看出，癌变区域的退偏值较大。从图6(b)、(d)可以看出，癌变区域的绝对相位值较大，即正常和癌变组织之间存在折射率差异，这对光学诊断来说是非常重要的。

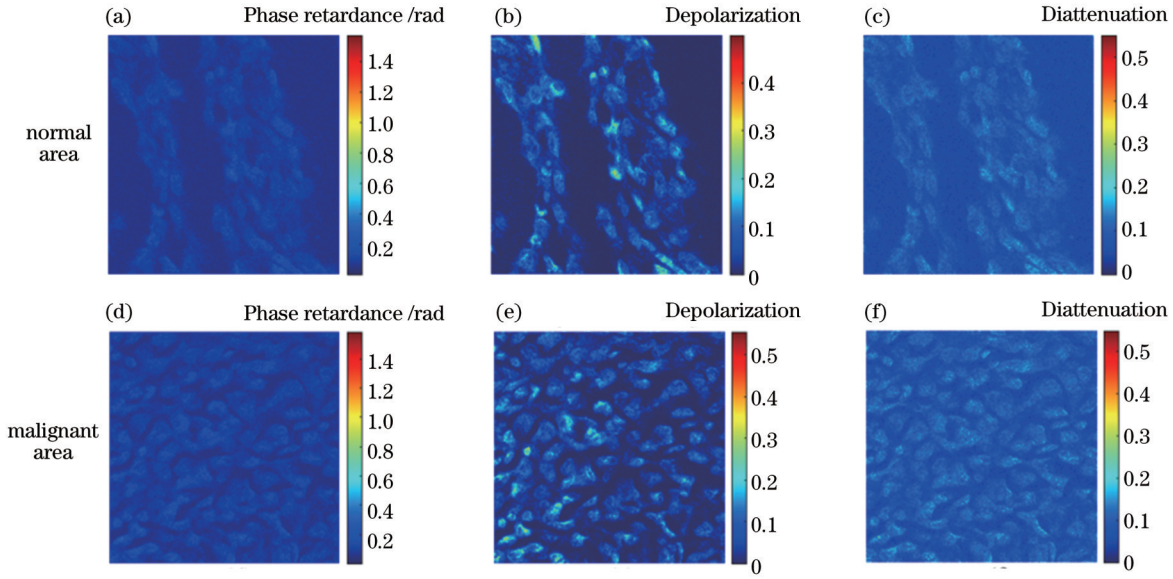

图 5 肺癌组织切片中正常区域和癌变区域的Mueller极分解图像。(a)(d)相位延迟;(b)(e)退偏;(c)(f)双向衰减

Fig. 5 Mueller polar decomposition images of normal and malignant areas in lung cancer tissue section. (a)(d) Phase retardance; (b)(e) depolarization; (c)(f) diattenuation

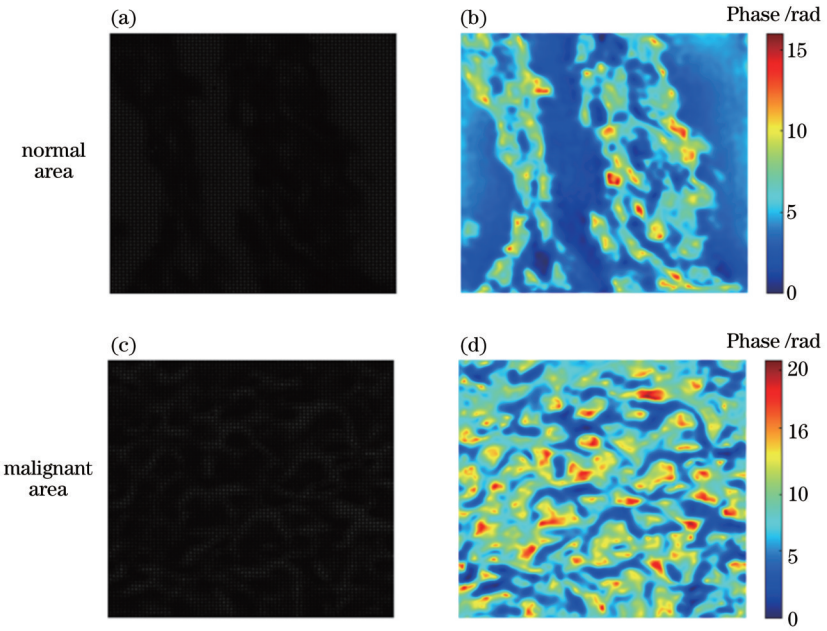

图 6 肺癌组织切片中正常区域和癌变区域的干涉图和相位图像。(a)(c)强度像;(b)(d)相位像

Fig. 6 Interference and phase images of normal and malignant areas in lung cancer tissue section. (a)(c) Interference image; (b)(d) phase image

因为在可见光谱范围内,组织的散射与吸收随波长的增加而减小,故红光是偏振探测的理想波段[34]。表 1 显示了当波长为 633 nm 时,正常和癌变区域中各 10 个位置处偏振极分解后的退偏参数均值的定量统计结果。可以看出,恶性肿瘤区域较正常区域细胞增多,且无论是整体图像还是单个细胞,恶性肿瘤区域的退偏值都高于正常区域。因此,退偏参数有可能成为区分肺癌切片中不同类型细胞的标准。表 2 定量显示了不同波长下,正常区域和癌变区域的绝对相位和折射率值。可以看出:无论是哪个波段,恶性肿瘤区域细胞的折射率值均大于正常区域;在 600、633、700 nm 三个波长处测量的正常区域细胞的折射率分别为 1.383、1.384、1.377,而恶性肿瘤区域中的细胞折射率分别为 1.518、1.516、1.511,与文献[26]中测量的折射率值基本一致。综上可见,偏振极分解的退偏参数和绝对相位推导的折射率值可以用来判断组织是否发育异常或是否发生了早期癌变。

表1 肺癌组织切片中正常区域和癌变区域退偏参数的统计分析

Table 1 Statistical analysis of depolarization parameters for normal and malignant areas in lung cancer tissue section

Region	Cell number	Depolarization of entire image /10^4	Depolarization of single cell /10^2
Normal	34-44	1.6	4
Malignant	52-58	3.3	6

表2 不同波长下肺癌组织切片中正常区域和癌变区域的绝对相位和折射率值

Table 2 Absolute phases and refractive indexes for normal and malignant areas in lung cancer tissue section under different wavelengths

Wavelength /nm	Normal region		Malignant region	
	Absolute phase /rad	Refractive index	Absolute phase /rad	Refractive index
600	16.04	1.383	21.69	1.518
633	15.22	1.384	20.48	1.516
700	13.53	1.377	18.34	1.511

4 结 论

研制的嵌入式相位传感的Stokes-Mueller成像偏振仪解决了传统Mueller矩阵偏振仪测量结果中绝对相位缺失的问题，通过测量绝对相位实现了样品折射率的测量，为癌症诊断提供了新的定量诊断指标。以肺癌切片为研究对象，实验结果表明，癌变区域的退偏参数和折射率值均大于正常区域，可实现对正常区域和癌变区域的区分。所研制的仪器不仅可以提取出偏振参数，还能定量得出组织的折射率信息，进一步拓展了传统Mueller偏振成像的功能。将偏振信息和相位信息相结合可以为癌症诊断提供更全面的定量评价指标，在未来有望利用计算机辅助研究人员进行指标初筛，体现了其在病理诊断研究中的应用潜力。

参 考 文 献

[1] Qi J, Elson D S. Mueller polarimetric imaging for surgical and diagnostic applications: a review[J]. Journal of Biophotonics, 2017, 10(8): 950-982.

[2] 王文爱, 马紫瑜, 李佳蓓, 等. Mueller成像偏振仪在病理诊断中的可靠性研究[J]. 光学学报, 2022, 42(15): 1512002.
Wang W A, Ma Z Y, Li J B, et al. Research on the reliability of Mueller imaging polarimeter in pathological diagnosis[J]. Acta Optica Sinica, 2022, 42(15): 1512002.

[3] 廖延彪. 偏振光学[M]. 北京: 科学出版社, 2003: 121-125.
Liao Y B. Polarization optics[M]. Beijing: Science Press, 2003: 121-125.

[4] Shukla P, Pradhan A. Mueller decomposition images for cervical tissue: potential for discriminating normal and dysplastic states[J]. Optics Express, 2009, 17(3): 1600-1609.

[5] Pierangelo A, Nazac A, Benali A, et al. Polarimetric imaging of uterine cervix: a case study[J]. Optics Express, 2013, 21(12): 14120-14130.

[6] Du E, He H H, Zeng N, et al. Mueller matrix polarimetry for differentiating characteristic features of cancerous tissues[J]. Journal of Biomedical Optics, 2014, 19(7): 076013.

[7] Yaroslavsky A N, Neel V, Anderson R R. Fluorescence polarization imaging for delineating nonmelanoma skin cancers [J]. Optics Letters, 2004, 29(17): 2010-2012.

[8] Wang Y, He H H, Chang J T, et al. Mueller matrix microscope: a quantitative tool to facilitate detections and fibrosis scorings of liver cirrhosis and cancer tissues[J]. Journal of Biomedical Optics, 2016, 21(7): 071112.

[9] Dubreuil M, Babilotte P, Martin L, et al. Mueller matrix polarimetry for improved liver fibrosis diagnosis[J]. Optics Letters, 2012, 37(6): 1061-1063.

[10] Oldenbourg R. A new view on polarization microscopy[J]. Nature, 1996, 381(6585): 811-812.

[11] Oldenbourg R. Polarized light microscopy: principles and practice [J]. Cold Spring Harbor Protocols, 2013, 2013(11): 078600.

[12] de Martino A, Kim Y K, Garcia-Caurel E, et al. Optimized Mueller polarimeter with liquid crystals[J]. Optics Letters, 2003, 28(8): 616-618.

[13] Novikova T, Pierangelo A, de Martino A, et al. Polarimetric imaging for cancer diagnosis and staging[J]. Optics and Photonics News, 2012, 23(10): 26-33.

[14] Vizet J, Manhas S, Tran J, et al. Optical fiber-based full Mueller polarimeter for endoscopic imaging using a two-wavelength simultaneous measurement method[J]. Journal of Biomedical Optics, 2016, 21(7): 71106.

[15] Pierangelo A, Manhas S, Benali A, et al. *Ex vivo* photometric and polarimetric multilayer characterization of human healthy colon by multispectral Mueller imaging[J]. Journal of Biomedical Optics, 2012, 17(6): 066009.

[16] Wang J Z, Li Y Q, Cao C L, et al. High-fidelity and rapid cellular-level Mueller matrix imaging for tissue identification with unstained sections[J]. Biomedical Optics Express, 2021, 12 (8): 4745-4758.

[17] 李华贵, 李艳秋, 郑猛. 癌变对上皮组织前后向散射特性影响的对比研究[J]. 光学技术, 2018, 44(2): 211-215.
Li H G, Li Y Q, Zheng M. Comparative study of influence of canceration on forward and backward scattering characteristics of epithelial tissues[J]. Optical Technique, 2018, 44(2): 211-215.

[18] 李艳秋, 周国栋, 李建慧, 等. 一种Stokes-Mueller光谱成像系统和检测方法: CN110763341B[P]. 2021-07-16.
Li Y Q, Zhou G D, Li J H, et al. Stokes-Mueller spectral imaging system and detection method: CN110763341B[P]. 2021-07-16.

[19] Cao C L, Wang J Z, Zhou G D, et al. Quantitatively characterizing the microstructural features of collagen fiber bundles with or without tenocytes by Mueller imaging polarimeter[J]. Proceedings of SPIE, 2021, 11925: 119250Z.

[20] Li J H, Li Y Q, Liu K, et al. Hybrid calibration method of a wide-view-angle Mueller polarimeter for hyper-numerical-aperture imaging systems[J]. Chinese Optics Letters, 2020, 18 (8): 081202.

[21] He C, He H H, Chang J T, et al. Characterizing microstructures of cancerous tissues using multispectral transformed Mueller matrix polarization parameters[J]. Biomedical Optics Express, 2015, 6(8): 2934-2945.

[22] 黄彤宇, 孟若愚, 赵千皓, 等. 模块化全偏振显微镜[J]. 中国激光, 2021, 48(15): 1517002.

Huang T Y, Meng R Y, Zhao Q H, et al. Modular full-polarization microscope[J]. Chinese Journal of Lasers, 2021, 48(15): 1517002.

[23] 何宏辉, 曾楠, 廖然, 等. 偏振光成像技术用于肿瘤病变检测的研究进展[J]. 生物化学与生物物理进展, 2015, 42(5): 419-433.
He H H, Zeng N, Liao R, et al. Progresses of polarization imaging techniques and their applications in cancer detections[J]. Progress in Biochemistry and Biophysics, 2015, 42(5): 419-433.

[24] Sun M H, He H H, Zeng N, et al. Characterizing the microstructures of biological tissues using Mueller matrix and transformed polarization parameters[J]. Biomedical Optics Express, 2014, 5(12): 4223-4234.

[25] 杜娥. 偏振散射特征定量检测与组织病变诊断机理研究[D]. 北京: 清华大学, 2014: 11-14.
Du E. A study on quantitative polarization characterization of tissues for diagnosis applications[D]. Beijing: Tsinghua University, 2014: 11-14.

[26] Bolin F P, Preuss L E, Taylor R C, et al. Refractive index of some mammalian tissues using a fiber optic cladding method[J]. Applied Optics, 1989, 28(12): 2297-2303.

[27] 杨泽文, 张璐, 吕宁, 等. 生物折射率三维无标记定量成像研究进展[J]. 中国激光, 2022, 49(5): 0507201.
Yang Z W, Zhang L, Lü N, et al. Progress of three-dimensional, label-free quantitative imaging of refractive index in biological samples[J]. Chinese Journal of Lasers, 2022, 49(5): 0507201.

[28] 韩冰, 周文静, 李海鹏, 等. 三视角数字全息层析重建光纤折射率实验研究[J]. 光学学报, 2013(s2): s209001.
Han B, Zhou W J, Li H P, et al. Reconstruction of refractive index of optical fiber by digital holographic tomography based on three-angle projections[J]. Acta Optica Sinica, 2013(s2): s209001.

[29] 刘克, 王健年, 李艳秋. 一种基于全局随机编码规则的混合衍射光栅: CN108761605B[P]. 2021-05-04.
Liu K, Wang J N, Li Y Q. Hybrid diffraction grating based on global random coding rule: CN108761605B[P]. 2021-05-04.

[30] Ling T, Jiang J B, Zhang R, et al. Quadriwave lateral shearing interferometric microscopy with wideband sensitivity enhancement for quantitative phase imaging in real time[J]. Scientific Reports, 2017, 7: 9.

[31] Khadir S, Bon P, Vignaud D, et al. Optical imaging and characterization of graphene and other 2D materials using quantitative phase microscopy[J]. ACS Photonics, 2017, 4(12): 3130-3139.

[32] Wang L, Liu K, Li Y Q. Quality map guided parallel phase unwrapping algorithm for multi-lateral shearing interferometry [J]. Proceedings of SPIE, 2021, 11927: 119270R.

[33] 张婷, 路元刚, 张旭苹. 基于边缘检测的最小不连续相位展开算法[J]. 光学学报, 2009, 29(1): 180-186.
Zhang T, Lu Y G, Zhang X P. Minimum-discontinuity phase unwrapping algorithm based on edge detection[J]. Acta Optica Sinica, 2009, 29(1): 180-186.

[34] 高瑞娟, 王春华, 宁金星, 等. 基于Mueller矩阵的生物细胞偏振显微成像[J]. 激光与光电子学进展, 2021, 58(18): 1811023.
Gao R J, Wang C H, Ning J X, et al. Polarization microscopy imaging of biological cells based on Mueller matrix[J]. Laser & Optoelectronics Progress, 2021, 58(18): 1811023.

Multifunctional Stokes-Mueller Polarimeter Based on Embedded Phase Sensing

Zhong Hui, Li Yanqiu**, Liu Ke*, Wang Jiazhi, Li Yuanhe, Wu Jinxian

Key Laboratory of Photoelectronic Imaging Technology and System, Ministry of Education, School of Optics and Photonics, Beijing Institute of Technology, Beijing 100081, *China*

Abstract

Objective Since polarization imaging technology can extract richer structural and optical information of samples and is highly sensitive to changes in subwavelength microstructures, it has a bright application prospect in biomedicine. The Mueller matrix has been widely used in the pathological diagnosis of cancers because it can quantitatively provide complete polarization information of biomedical specimens. However, the existing Mueller imaging polarimeter loses the absolute phase information of the sample, and the relative phase information cannot reflect the change law of the phase to be measured. Absolute phase, as a basic property of light, quantifies the phase characteristics determined by the physical thickness and refractive index coefficient of the sample and reflects the changes to be measured. As one of the most important optical properties of biological samples, the refractive index has been proven to be useful for describing the optical properties of biological tissues and evaluating pathological tissues. As an absolute-phase detection method, the quadriwave lateral shearing interferometer is highly suitable for phase microscopic imaging and the measurement of absolute phase information of samples due to its advantages, such as no need for additional wavefront reference beam, no special requirements on the light source, and simple structure. However, the applications of the quadriwave lateral shearing interferometer in the pathological diagnosis of cancer tissues are rarely reported. Therefore, an embedded absolute-phase detection instrument needs to be developed to meet the detection requirements of different types of samples.

Methods As the existing Mueller imaging polarimeter loses the absolute phase information of the sample, a multifunctional Stokes-Mueller polarimeter based on embedded phase sensing is built. Specifically, the analysis of the polar decomposition equation for the Mueller matrix shows that the Mueller matrix does not retain the absolute phase

information of the polarized light, but only contains the phase delay information of polarized light. Then, the self-developed quadriwave lateral shearing interferometer is integrated into the polarimeter. A multifunctional Stokes-Mueller polarimeter based on embedded phase sensing is thereby obtained, and it solves the problem of missing absolute phase in the measurement results obtained by the Mueller matrix polarizer. Finally, the phase distribution of the sample is reconstructed by MATLAB according to the collected interferogram, and the refractive index is calculated. With a lung cancer tissue section as the research object, in addition to the extraction of polarization information of the biological sample, the refractive index is measured on the basis of the absolute-phase value. This instrument can serve as a new quantitative diagnostic index and enrich the measurement function of the polarizer.

Results and Discussions The multifunctional Stokes-Mueller polarimeter based on embedded phase sensing is applied to the measurement of a lung cancer tissue section. 10 positions are selected from the normal and malignant areas for polarization and phase measurement, respectively. The results show that the morphology and arrangement of cells in different areas are not the same. In the malignant area, the arrangement of cells is disorderly, and the number of cells increases exceptionally due to excessive proliferation. Quantitative analysis shows that the depolarization and absolute-phase values of the malignant area are both large. That is, normal and malignant tissues have different refractive indexes, and this is crucial for optical diagnosis (Figs. 5 and 6). The malignant area has more cells than the normal area, and it also has a depolarization value higher than that of the normal area in both the whole image and a single cell (Table 1). The refractive index values of the cells in the malignant area measured at the wavelengths of 600, 633, and 700 nm are all larger than those of the cells in the normal area. To be precise, the refractive index values of the cells in the normal area measured at the three wavelengths are 1.383, 1.384, and 1.377, respectively, while those of the cells in the malignant area are 1.518, 1.516, and 1.511, respectively (Table 2). Therefore, depolarization parameters of polarization decomposition and the refractive index derived from the absolute phase can be used to determine whether a tissue is abnormal or early cancerous.

Conclusions The multifunctional Stokes-Mueller polarimeter based on embedded phase sensing solves the problem of missing absolute phase in the measurement results obtained by the Mueller matrix polarizer. The refractive index of the sample is measured on the basis of the absolute phase, and it can serve as a new quantitative diagnostic index for cancer diagnosis. An experiment is conducted with a lung cancer tissue section as the research object, and the results show that the depolarization parameter and refractive index of the malignant area are all larger than those of the normal area. The distinction between the normal and malignant areas can thus be achieved. The developed instrument can not only extract polarization parameter, but also quantify the refractive index information of the tissue. In this way, it further expands the functions of the traditional Mueller polarimetric imager. The combination of polarization information and phase information can provide a more comprehensive quantitative evaluation index for cancer diagnosis. In the future, this instrument can assist researchers in the preliminary screening of indicators, which reflects the application potential of the proposed instrument in pathological diagnosis research.

Key words measurement; polarization; Mueller matrix; phase measurement; refractive index; quantitative